ELSEVIER

Catalysis Today 68 (2001) 227–236

CATALYSIS TODAY

www.elsevier.com/locate/cattod

Nanoparticles of 3d transition metal oxides in mesoporous MCM-48 silica host structures: Synthesis and characterization

Ralf Köhn [a], Michael Fröba [a,b,*]

[a] *Institute of Inorganic and Applied Chemistry, University of Hamburg, Martin-Luther-King-Platz 6, D-20146 Hamburg, Germany*
[b] *Institute of Inorganic and Analytical Chemistry, Justus-Liebig-University Giessen, Heinrich-Buff-Ring 58, D-35392 Giessen, Germany*

This work is dedicated to Prof. Dr. Wolfgang Metz on the occasion of his 65th birthday

Abstract

Transition metal oxide nanoparticles were synthesized within mesoporous MCM-48 silica phases. By wet impregnation, drying, and calcination procedures, it was possible to form iron, iron/cobalt, cobalt, nickel, and copper oxide nanoparticles almost exclusively within the pore system. Nitrogen sorption measurements still revealed mesoporosity for the host/guest compounds accompanied by a reduction of the surface area and pore radius, both indications of a decoration/coating of the inner surface of the silica walls. X-ray absorption spectroscopic measurements proved the existence of small, slightly disordered metal oxide nanoparticles. HRTEM investigations showed that the mesoporous host structure was still intact after the treatment. Thermogravimetric investigations revealed differences in the reduction/oxidation behavior of the metal oxide nanoparticles compared to their corresponding bulk phases.

Keywords: MCM-48 silica phase; Transition metal oxide; Nanoparticles

1. Introduction

The discovery of ordered mesoporous molecular sieves (denoted as M41S family) [1,2] has expanded the range of uniform pore sizes from the micropore to the mesopore regime. Great attention arised from that for different fields of materials science, i.e. catalysis [3,4], nanostructured host/guest compounds [5,6], and sorption materials [7–15]. Originally, this family has been classified into three subgroups: a hexagonal (MCM-41), a cubic (MCM-48) and a lamellar phase (MCM-50).

In contrast to the hexagonal MCM-41 silica phase with its one-dimensional (1d) channel system, we have focused our work on the cubic MCM-48 phase, which has the great advantage of a 3d pore system. The surface-defining MCM-48 silica is the gyroid or G-surface, forming a structure with the space group $Ia\bar{3}d$ [16–18], which is frequently observed in water-surfactant systems [19–21]. The structure contains a 3d network with channels running along [1 1 1] and [1 0 0], which provides large surface areas and a high accessibility of sites within the porous network structure even if part of the pore entrances cannot be used due to blockage. In comparison to MCM-41, the synthesis of MCM-48 is more difficult, which is the reason, why only few groups have focused their efforts on this particular cubic phase in the beginning [22–25]. Due to its special pore structure, the mesoporous MCM-48 phase is very interesting

* Corresponding author. Tel.: +49-641-99-34100; fax: +49-641-99-34109.
E-mail address: michael.froeba@anorg.chemie.uni-giessen.de (M. Fröba).

0920-5861/01/$ – see front matter
PII: S0920-5861(01)00282-6

as a matrix to immobilize catalytically active metal species [26–28], e.g. Ti [29–34], V [35,36], Cr [37], Mn [38,39], Al [40–42], Fe [43], Cu [44,45], and Zr [46], onto or within the silica walls or as a host to accommodate nanostructured guest compounds [47,48].

There are two different ways [46] to introduce catalytic active sites into the mesoporous MCM-48 system: (i) adding the metal ions to the synthesis gel of the MCM-48 silica phase prior to the hydrothermal treatment or (ii) by post-synthetic incorporation. The disadvantage of the first method is a lower long-range order of the final material due to distortion of the liquid crystalline template by the metal ions during the synthesis.

The advantage of the post-synthetic treatment is the opportunity to start with a highly ordered mesoporous material with a very high inner surface. There are two different ways for the post-synthetic treatment: grafting of precursor species from the gas phase or by wet impregnation technique. Gas phase introduction usually results in low loadings, but without any affection of the porous host. The wet impregnation technique, however, allows higher degrees of loading, but requires a very careful preparation, otherwise the host structure can be destroyed.

The main problem in all cases is the characterization of the products and particularly the chemical nature of the nanostructured guest compounds. The combination of comprehensive characterization techniques, i.e. powder X-ray diffraction (PXRD), high resolution transmission electron microscopy (HRTEM), selected area electron diffraction (SAED), energy dispersive spectroscopy (EDS), nitrogen physisorption is necessary to prove that most of the catalytic metal species are inside the porous host structure. To characterize the metal species itself, techniques like IR-, UV/VIS-spectroscopy, thermogravimetry investigations coupled with differential thermal analysis and mass spectroscopy (TG/DTA/MS) and X-ray absorption spectroscopy (XAS) have to be applied.

In this study we focused our work on the intrapore formation of the late 3d transition metal oxides (binary iron, cobalt, nickel, copper and ternary cobalt iron oxides) within the mesopores of the MCM-48 silica species [45,48–50]. The chosen metals are of high interest due to their wide range of application in catalysis, e.g. NO_x reduction, Fischer–Tropsch synthesis or methanol decomposition.

2. Experimental

The syntheses of the pristine MCM-48 silica materials were carried out by mixing reactants with the following composition: 1.0 tetraethylorthosilicate (TEOS):0.65 cetyltrimethylammonium bromide (CTAB):0.5KOH:62H_2O. For a pre-hydrolization of the TEOS, the CTAB was added after 10 min of vigorous stirring. Stirring was continued for additional 20–30 min to homogenize the synthesis mixture. In a teflon-lined steel autoclave under hydrothermal conditions (388 K), the condensation of the silica was performed for 48–72 h. The resultant white product was filtered and washed several times with deionized water. After drying, it was calcined at 773–823 K (heating ramp of 1 K min^{-1}) in air for 6 h within a programmable furnace of the company GERO type F 40-500/1300C. The obtained pristine MCM-48 silica are of high quality and thermal stability up to 923 K in air if the samples are thoroughly dried. Total removal of template by calcination procedure was proved by FTIR exhibiting no corresponding C–C, C–H, C–N bands. The formation of the binary metal oxides (Fe, Co, Ni, Cu) onto the inner surface of MCM-48 was carried out by the wet impregnation technique with 1.6 M aqueous solution of transition metal nitrate, or a mixture of iron and cobalt nitrates with a ratio of 1Co:2Fe, respectively [50]. In case of the iron nitrates different loading was gained by impregnation with 0.07, 0.37, and 1.18 M aqueous solutions. After impregnation the resulting product was dried at room temperature under vacuum for more than 5 h. Afterwards the material was calcined at 673 (iron oxides, cobalt oxides), 773 (nickel oxides, copper oxides), 873 and 923 K (iron cobalt oxide) under air for 6 h, which led to a transformation of the metal nitrate into an oxide as indicated by the disappearance of the IR band of the NO_3^- ion at 1380 cm^{-1}.

Powder X-ray diffraction patterns were recorded with a Bruker/AXS D8 advance diffractometer using filtered Cu Kα radiation in θ/θ geometry. The diffractometer was equipped with variable slits on the tube and detector side and a secondary monochromator.

The data were taken in a step scan mode with 0.02°θ and a counting time of 1 s per step.

The specific surface areas and pore diameters were determined by nitrogen adsorption/desorption isotherms, which were recorded at 77 K using an Autosorb 1 (Quantachrome). Before the physisorption measurements, the samples were outgassed at 373–423 K for 15–24 h. The surface areas were calculated applying the theoretic equation of Brunauer, Emmet and Teller (BET) for the relative pressures between 0.05 and 0.15–0.23, depending on the number of points that were appropriate for a linear fit. The pore size distributions were calculated using the desorption branch of the N_2 adsorption/desorption isotherm and the Barrett–Joyner–Halenda (BJH) formula [51].

X-ray absorption spectroscopic measurements were carried out at the storage ring DORIS III (HASYLAB@DESY, Hamburg, Germany) at the EXAFS II beam line, which was equipped with a Si(1 1 1) double-crystal monochromator. The Fe–K, Co–K, Ni–K, and Cu–K edge spectra were recorded at room temperature in transmission mode; except for the Fe–K edge spectra of the binary iron oxide MCM-48 silica materials, which were taken at 20 K. Each spectrum was calibrated against the first inflection point of the corresponding K edge of a metal foil, which was measured simultaneously. As reference for the guest compounds, the freshly prepared corresponding metal oxides were used. All samples were measured as pressed polyethylene pellets in which the transition metal content was adjusted to give an absorption jump $\Delta\mu d = 0.4$–0.9. For further data analyses, the program WinXAS [52] was used. Theoretical calculations of the phase shifts and backscattering amplitudes were calculated using FEFF6.01 [53].

For electron microscopic measurements the powders were crushed in ethanol and the ground material was dispersed on a holly carbon grid. The HRTEM studies were carried out using a Philips CM20 operating at 200 kV with a very low illumination to avoid destruction of the material under the electron beam. EDS analyses were performed using a Link QX 20 analytical system.

Thermogravimetric investigations were carried out with a Netzsch STA 409C/MS. This machine is connected via a capillary system 403/4 to a Balzers quadrupole mass spectrometer QMS 421, which needs an inert carrier gas. The reduction of bulk and nanostructured transition metal oxides was achieved with a gas mixture of 5% hydrogen in 95% nitrogen with a heating rate of 5 K min^{-1}.

3. Results and discussion

3.1. Powder X-ray diffraction

Powder X-ray diffraction is one of the main characterization methods for mesoporous materials of the M41S type and nanostructured host/guest compounds, respectively. The presence of guest species within the mesoporous structure can be detected by a reduction of the intensities of the M41S-typical Bragg reflections in PXRD [48,54]. In general, the introduction of scattering material into the pores leads to an increased phase cancellation between scattering from the wall and the pore regions and therefore to reduced scattering intensities for the Bragg reflections. Theoretical models have shown that this phase relationship is very sensitive. The degree of cancellation is mainly determined by the scattering contrast between the framework walls and the pores [55].

Fig. 1 shows the reduction of the typical reflections of a pristine MCM-48 silica material (A) after the impregnation and calcination with iron nitrate solutions of different concentration (0.07 mol l^{-1} B, 0.37 mol l^{-1} C, and 1.18 mol l^{-1} D). The increasing destructive interferences by the pore filling with rising amounts of the iron oxide are visible. Besides the typical MCM-48 silica reflections, no additional peaks are observed in the higher 2θ range. This indicates that no crystalline iron oxide phase (e.g. haematite d_{104} (100%) = 2.7 Å corresponding to 33.2°2θ) has been formed outside the pore structure.

Similar results are obtained for nickel and copper oxides within the mesoporous host structure. The only difference occurs by the intrapore formation of cobalt or cobalt iron oxide within the mesopores of the MCM-48 silica materials. Very broad high order Bragg reflections can be observed beyond $2\theta = 30°$. These reflections can be attributed to nanoparticles of inverse spinel systems like Fe_3O_4 and $CoFe_2O_4$ [50]. A rough estimation of the crystallite size by applying the Scherrer formula leads to particles of ca. 5–6 nm in diameter.

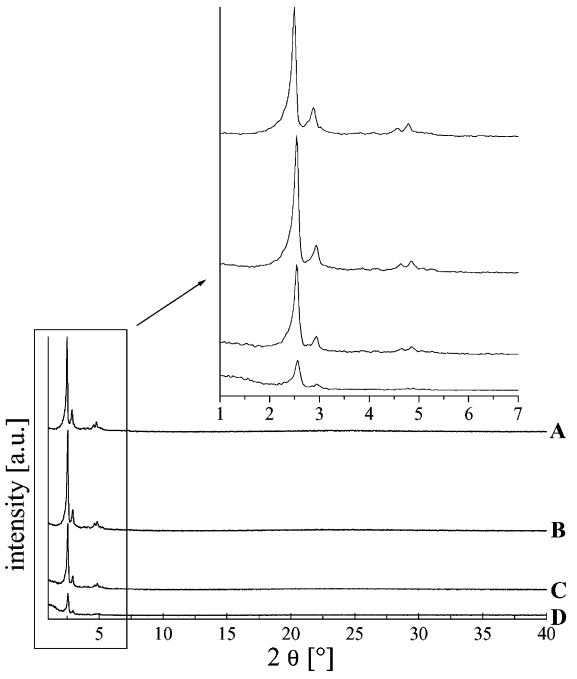

Fig. 1. PXRD patterns of pristine MCM-48 silica material (A) and after the impregnation/calcination treatment with 0.07 (B); 0.37 (C) and 1.18 (D) M aqueous iron nitrate solution. The enlargement shows the typical MCM-48 silica pattern, its reduction with increasing iron content, respectively.

The most sensitive step in the synthesis of the host/guest compounds by the wet impregnation/calcination technique is the drying procedure after the impregnation. Best results are obtained if the drying process is finished at room temperature and under vacuum. Every attempt to use elevated temperatures (above 300 K) leads to the premature formation of large transition metal oxide particles outside of the pores as proved by the respective PXRD patterns (not depicted).

3.2. Nitrogen physisorption

Besides PXRD, nitrogen physisorption is the method of choice to characterize mesoporous materials. This method gives information upon the specific surface area and the mean pore diameter. Although the applied theories for the calculation of the pore diameters of small mesopores (<5 nm) are still not perfect, they can be used to give proper information about the differences between different mesoporous materials. Calculations of mean pore diameter of mesoporous materials on the basis of the BJH theory are common. These calculations are based on the Kelvin equation and underestimate the mean pore diameter of small mesopores in the magnitude of at least 1 nm [56]. Nevertheless, comprehensive studies have shown that BJH compared to other theories for pore size calculations like Saito–Foley (SF) [57,58] or density functional theory (DFT) give appropriate results to determine the differences between pristine and modified MCM-48 silica materials [14,15].

As a representative example Fig. 2 shows the adsorption/desorption branches (a) and the mean pore diameter distribution calculated by BJH (b) of the pristine MCM-48 silica A and the three with iron oxide loaded materials B, C, and D. All materials show typical type IV isotherms (IUPAC classification [59]) as it is expected for mesoporous systems. Between p/p_0 0.2–0.3 a well-defined step occurs, representing the spontaneous filling of the mesopores due to capillary condensation. The amount of physisorbed nitrogen decreases with increased loading of the mesopores (B–D). The inflection point of the respective steps is shifted to lower values of p/p_0 as expected for smaller pores. The reduction of the mean pore diameter is observable in the pore diameter distribution, too (Fig. 2b). Besides the reduction of the mean pore diameter, a slight broadening of the distribution can be observed. This is probably due to a slight inhomogeneous filling/coating of the mesopores.

As all 3d metal oxide containing MCM-48 silicas still show mesoporosity, we can assume that the coating of the inner surface of the MCM-48 silica was successfully. Nevertheless, no complete filling of the pores could be observed in any case of the host/guest compound. A summary of the reduction of the specific surface areas S_{BET,N_2} and mean pore size diameters d_{p,N_2} (BJH) from the pristine MCM-48 silicas and the respective host/guest compounds is given in Table 1. There are two different effects causing a reduction of the specific surface area. First of all the intrapore formation of the transition metal oxide nanoparticles within the mesopores reduces the mean pore diameter and second the specific surface area itself, too. The latter effect is due to definition of the unit for the specific surface area d_{p,N_2} (BJH) $m^2\,g^{-1}$ [48].

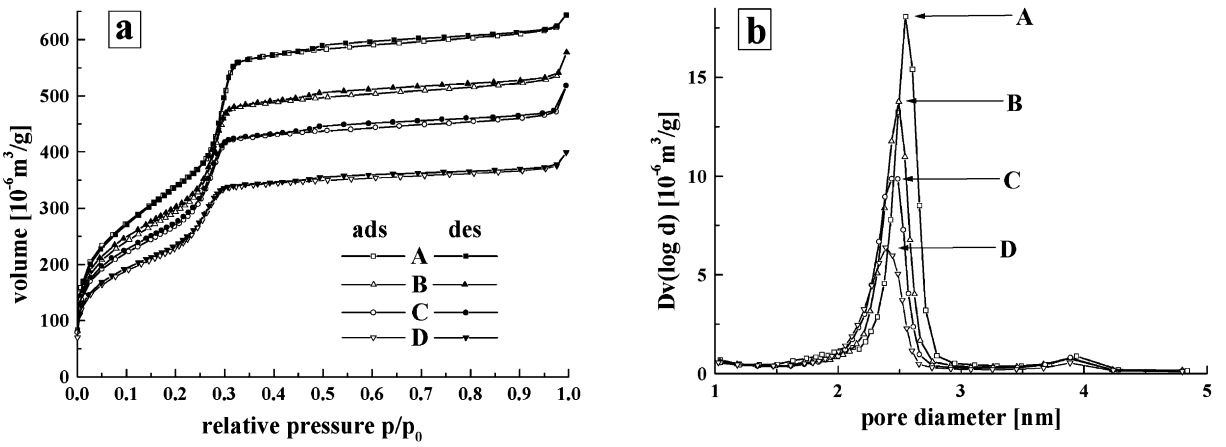

Fig. 2. (a) Nitrogen adsorption/desorption isotherms and (b) pore diameter distributions of pristine MCM-48 silica material (A) and after the impregnation/calcination treatment with 0.07 (B); 0.37 (C) and 1.18 (D) M aqueous iron nitrate solution.

3.3. Transmission electron microscopy

Transmission electron microscopy (TEM) is another method to prove the preservation of the mesoporous structure of the MCM-48 silicas upon the intrapore formation of the transition metal nanoparticles. Fig. 3 shows, as an example, the HRTEM photograph of a MCM-48 silica phase with an iron oxide content of 30 wt.%. This sample was prepared by two impregnation/calcination procedures to gather a high loading of iron oxide within the mesopores. The view along the ⟨1 1 0⟩ zone axis shows the perfect order over a large length scale (300 nm). This proves the outstanding long-range order of the MCM-48 silica material

Table 1
Nitrogen physisorption data for different pristine MCM-48 silica materials and the corresponding transition metal oxide containing phases[a]

Sample	S_{BET,N_2} ($m^2\,g^{-1}$)	d_{p,N_2} (BJH) (nm)
Pristine MCM-48 silica A	1273	2.55
Iron oxide/MCM-48 silica B	1093	2.47
Iron oxide/MCM-48 silica C	993	2.43
Iron oxide/MCM-48 silica D	836	2.37
Pristine MCM-48 silica	1106	2.52
Cobalt oxide/MCM-48 silica	718	2.38
Pristine MCM-48 silica	1217	2.48
Cobalt iron oxide/MCM-48 silica	593	2.21
Pristine MCM-48 silica	1133	2.68
Nickel oxide/MCM-48 silica	734	2.59
Copper oxide/MCM-48 silica	678	2.58

[a] S_{BET,N_2}: total surface area by BET theory; d_{p,N_2} (BJH): mean pore diameter by BJH calculation.

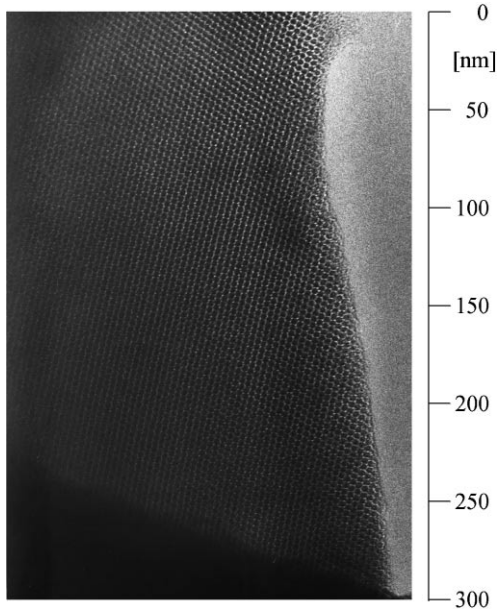

Fig. 3. Representative HRTEM photograph of MCM-48 silica materials with 30% iron oxide within the mesopores (⟨1 1 0⟩ zone axis).

even after wet impregnation and calcination at 673 K. This photograph is representative for a large number of different crystallites. EDS investigations revealed an almost homogeneous dispersion of iron oxide over the whole sample area although minor deviations in the intensity have to be stated [48,49].

3.4. X-ray absorption spectroscopy (XAS)

The formation of the transition metal oxides located within the mesoporous host structure of the MCM-48 silica material was proved by the characterization methods just mentioned above. However, there is still no information upon the structure of the nanostructured oxides itself. XAS [1] as an element-specific technique provides qualitative and quantitative information on the local structure, which is not accessible by methods like PXRD in case of these nanostructured host/guest compounds. Two representative results are shown here, first (part I) the quantitative examination of iron oxide nanoparticles within the MCM-48 silica host by extended X-ray absorption fine structure (EXAFS) analysis and second (part II) a qualitative solution of the structure problem for the ternary guest compound $CoFe_2O_4$ in MCM-48 silica.

3.4.1. State I

Refined structure parameters of the Fe–Fe coordination shells, which are extracted from the Fe–K EXAFS of the Fe_2O_3/MCM-48 host/guest compound with 30 wt.% iron oxide (already shown in Fig. 3) are listed in Table 2. Bulk haematite powder prepared by calcination from iron nitrate at the same temperature (673 K) was measured and refined too. The fourth column represents data from the structure analysis of haematite single crystals taken from the literature [60].

For data analysis the Fe–Fe coordination shells were extracted by Fourier filtering using a Bessel window ranging from $R = 2.3$–3.5 Å. Refined structure parameters were obtained by fitting the obtained back transformations (BTs) in k-space within the range of $k = 3.0$–$14.8\ Å^{-1}$ using three shells representing three different Fe–Fe linkages. In case of bulk haematite, four shells were used. To keep the number of independent parameters as small as possible during the refinements, some conditions with respect to the variables had to be made: (1) the amplitude reduction factor was always kept constant to one; (2) the energy shift ΔE_0 was the same for each shell and (3) the Debye–Waller factors were constrained within the range of 0.002–0.0045 $Å^2$.

Bulk haematite, which is isostructural with corundum, can be described as consisting of hcp arrays of oxygen ions with two-thirds of the octahedral sites filled with Fe(III) ions [61]. In case of crystalline haematite four different Fe–Fe coordination shells exist within the range of 2.9–3.7 Å (see Table 2). While the nearest (2.90 Å) and next-nearest (2.97 Å) neighbor shells are formed by face- and edge-shared octahedra, respectively, the other two (3.36 and 3.71 Å) are due to a corner-shared linkage.

To check the accuracy of the least-squares refinements, we also fitted the data of the bulk haematite, which were treated in the same way as the data of the nanostructured Fe_2O_3/MCM-48. The received results are in nice agreement with the values obtained from single-crystal XRD data as listed in Table 2 (fourth column).

In contrast to the bulk haematite, the first Fe–Fe shell of the nanoparticles appears at 3 Å, a distance that can only be formed by edge-shared octahedra. The host/guest compound does not contain any face-shared FeO_6 octahedra. In addition, the other two Fe–Fe shells of the nanoparticles occur at distances of ca. 3.12 and 3.46 Å, which corresponds to another edge- and a corner-shared linkage. The facts that no face-shared FeO_6 octahedra are found and that the coordination numbers for each shell are relatively small compared to those in haematite indicates the small size of the iron oxide nanoparticles within the mesopores of MCM-48. This is in agreement with the physisorption experiments and the microscopic investigations. It proves the coating of the mesopores with a very thin layer of iron oxide [48].

3.4.2. State II

The second example for the use of XAFS in a more qualitative way is given in Figs. 4 and 5. Cobalt iron oxide within the mesopores is formed via the impregnation with the 1:2 Co/Fe nitrate solution, which might lead to one of the following oxides: Fe_2O_3, Co_2O_3, Fe_3O_4, Co_3O_4 or $CoFe_2O_4$. As the calcination

[1] In modern nomenclature the abbreviation XAFS will be used too. XAFS represents the combination of the two regions of the absorption spectrum: X-ray absorption near-edge structure (XANES) and extended X-ray absorption fine structure (EXAFS).

Table 2
Refined structure parameters of the Fe–Fe coordination shells, extracted from the Fe–K EXAFS of Fe_2O_3/MCM-48 host/guest compounds, and bulk haematite[a]

	Sample		
	Nanostructured Fe_2O_3/ MCM-48 ($\Delta E_0 = 3.9$)	Bulk haematite powder ($\Delta E_0 = -1.6$)	Single crystal data for haematite [60]
Iron–iron shells			
N		0.91	1
R (Å)		2.91	2.90
$\Delta\sigma^2$ (Å^2)		0.0025	–
N	0.98	2.95	3
R (Å)	2.99	2.97	2.97
$\Delta\sigma^2$ (Å^2)	0.003	0.0039	–
N	1.12	2.80	3
R (Å)	3.13	3.37	3.36
$\Delta\sigma^2$ (Å^2)	0.003	0.0034	–
N	0.51	3.12	6
R (Å)	3.46	3.70	3.71
$\Delta\sigma^2$ (Å^2)	0.004	0.002	–

[a] N: coordination number; R: bond length; $\Delta\sigma^2$: Debye–Waller factor; ΔE_0: energy shift.

temperature for the formation of the oxides from the nitrates was 875 K, we can exclude all oxy hydroxides of iron and cobalt. A water uptake of the final products was not detected; post-synthetic formation of hydroxides can be excluded too. By PXRD it is known that an inverse spinel structure has been formed. From the phases just listed above only the Fe_3O_4, $CoFe_2O_4$ are of this type, Co_3O_4 forms a normal spinel structure.

Fig. 4 shows the X-ray absorption near edge structure (XANES) of the Co–K edge of the respective compounds (a) and the modified radial distribution functions (not phase-shift corrected) (mRDF) extracted from the corresponding EXAFS regions (b). As reference samples bulk Co_3O_4 and $CoFe_2O_4$ were used.

In the XANES region of the absorption spectra, which is like a fingerprint, the Co/Fe/O-MCM-48 compound has the same energy position for the edge as the one of the bulk $CoFe_2O_4$. Therefore, cobalt in the oxidation state II is present in bulk $CoFe_2O_4$ as well as in the nanostructured host/guest compound. In contrast, the reference compound Co_3O_4 contains two Co(III) ions for every Co(II), which is the reason for the shift of the absorption edge to higher energies.

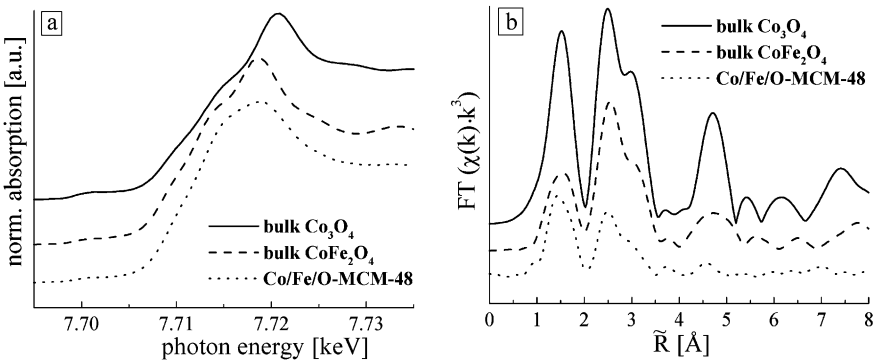

Fig. 4. (a) Co–K edge absorption jump and (b) mRDF of the Fe–K edge EXAFS oscillations for Co_3O_4, $CoFe_2O_4$, and mesoporous Co/Fe/O-MCM-48 silica material.

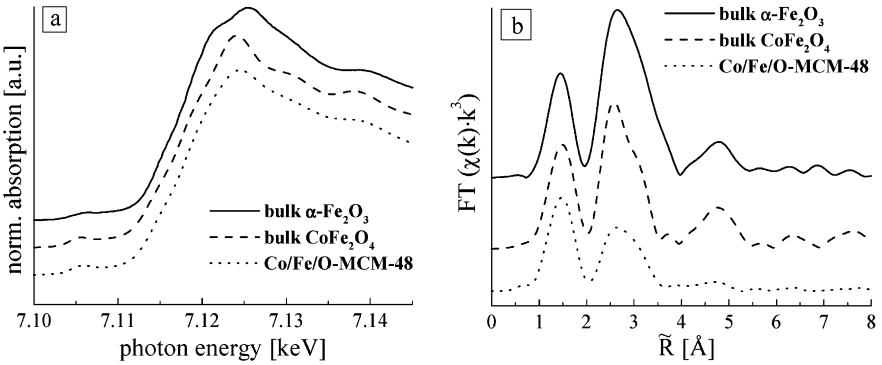

Fig. 5. (a) Fe–K edge absorption jump and (b) mRDF of the Fe–K edge EXAFS oscillations for Co_3O_4, $CoFe_2O_4$, and mesoporous Co/Fe/O-MCM-48 silica material.

The smearing out of the edge itself compared to the bulk $CoFe_2O_4$ is typical for nanostructured material and has been reported before [48,62].

In Fig. 4b showing the mRDF of the EXAFS investigation — the first oxygen shell of the nanostructured Co/Fe/O-MCM-48 compound is comparable in height to the $CoFe_2O_4$ reference material. In contrast, the first oxygen shell in the bulk Co_3O_4 is twice more in height. Another typical feature for nanostructured particles is the reduction of the higher metal–metal shells in the mRDF in comparison to the corresponding bulk materials as it is apparitional within 2–5.5 Å in Fig. 4b.

Similar features will be observed in Fig. 5, which shows the XANES and EXAFS results of the Fe–K absorption edges. The XANES of the two bulk references α-Fe_2O_3 and $CoFe_2O_4$ and the Co/Fe/O-MCM-48 silica material appear with the same valence shift representing the presence of iron in the oxidation state three exclusively. Again, the smearing out of the edge feature in the XANES spectra as well as the reduction of the higher shells in the mRDF can be observed.

These qualitative results for the structure of the Co/Fe/O-MCM-48 host/guest compound point to a cobalt ferrite ($CoFe_2O_4$) like structure for this materials, although a more quantitative evaluation of these data is currently in progress.

3.5. Thermogravimetric analyses

Thermogravimetric analyses of the redox stability of the transition metal oxide nanoparticles were carried out in comparison to their corresponding bulk phases. Bulk haematite can be easily reduced to magnetite at 673 K by a mixture of 5% hydrogen in 95% nitrogen. In contrast, nanostructured iron(III) oxide within the mesopores of the MCM-48 silica cannot be reduced under the same conditions. Raising the temperature above 700 K results in a reduction of iron(III) to iron(II), but at expense of the formation of the iron silicate fayalite (Fe_2SiO_4).

Copper oxide nanoparticles on the other hand can be reduced at lower temperatures following a different reaction way in comparison to their bulk phase as it is shown in Fig. 6. Again the reduction was

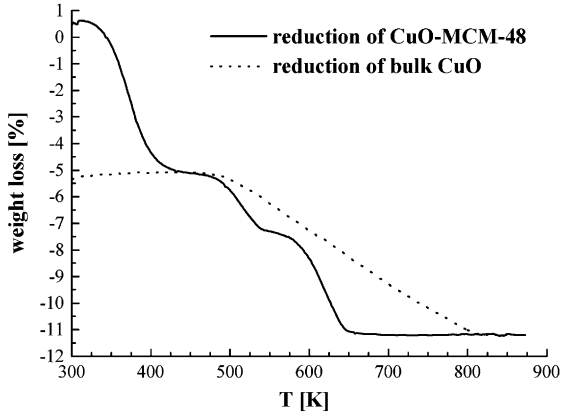

Fig. 6. Comparison of the weight loss of bulk and nanostructured CuO by reduction with H_2/N_2 (5:95%) with a heating rate of 5 K min^{-1}.

performed by a mixture of H_2/N_2 (5:95%) with a heating rate of $5\,K\,min^{-1}$. For an easier comparison the weight loss of bulk CuO has been rescaled to fit the one of CuO in the mesoporous MCM-48 silica matrix. The starting product was CuO and the final product was elementary copper as proved by XAFS investigations [45]. The nanostructured CuO phases first loses water in a temperature range of 300–420 K. Then, the reduction to copper metal starts at ca. 420 K in two steps. Typical for this type of CuO nanoparticles is the formation of Cu_2O at the end of the first step which ends at ca. 520 K. The second step runs from 560 to 640 K to copper metal. In contrast, the reduction of the bulk oxide to the metal starts at the same temperature of 450 K, but runs in one long step up to a much higher temperature of 800 K. This shows the much higher reactivity of the extremely well dispersed Cu nanoparticles within the mesoporous host structure compared to their corresponding bulk phase.

4. Conclusions

We have shown that wet impregnation/calcination procedure leads to highly dispersed nanoparticles within the mesopores of MCM-48 silica materials. Different loading with transition metal oxide nanoparticles can be obtained either by multiple impregnation/calcination cycles [48] or by different concentrations of the impregnation solution. The preservation of the mesoporous host structure remains intact even at calcinations temperatures of 923 K [50] as proved by PXRD, N_2 physisorption and electron microscopy. XAFS investigations allow the determination of the local structure of the nanoparticles formed within the mesoporous host. Thermogravimetric studies show differences in the reduction behavior of nanostructured copper oxides and their corresponding bulk phases. The difference in the reduction behavior of the nanostructured CuO within the mesoporous host structure is very promising for further possible catalytic applications. Its catalytic potential for methanol decomposition is currently being studied [63]. Investigations of the catalytic activity of the iron oxide nanostructures for the NO_x decomposition are in progress too.

Acknowledgements

We thank Dr. O. Richard and Prof. G. van Tendeloo of the University of Antwerp, Belgium, for the help on the electron microscopic investigations and Dr. S. Ebbinghaus for the support on the nickel and copper oxide materials. We thank Dr. M. Thommes (Quantachrome) for the helpful discussion. Financial support by the Deutsche Forschungsgemeinschaft (Fr 1372/1-1 and Fr 1372/42-2), the Fonds der Chemischen Industrie, and the University of Hamburg is gratefully acknowledged.

References

[1] C.T. Kresge, M.E. Leonowicz, W.J. Roth, J.C. Vartuli, J.S. Beck, Nature 359 (1992) 710.
[2] J.S. Beck, J.C. Vartuli, W.J. Roth, M.E. Leonowicz, C.T. Kresge, K.D. Schmitt, C.T.-W. Chu, D.H. Olson, E.W. Sheppard, S.B. McCullen, J.B. Higgins, J.L. Schlenker, J. Am. Chem. Soc. 114 (1992) 10834.
[3] A. Corma, Chem. Rev. 97 (1997) 2373.
[4] J.Y. Ying, C.P. Mehnert, M.S. Wong, Angew. Chem. Int. Ed. 38 (1999) 56.
[5] K. Moller, T. Bein, Chem. Mater. 10 (1998) 2950.
[6] L. Chen, P.J. Klar, W. Heimrodt, F. Brieler, M. Fröba, Appl. Phys. Lett. 76 (2000) 3531.
[7] P.J. Branton, P.G. Hall, K.S.W. Sing, J. Chem. Soc., Chem. Commun. (1993) 1257.
[8] P.J. Branton, P.G. Hall, K.S.W. Sing, H. Reichert, F. Schüth, K.K. Unger, J. Chem. Soc., Faraday Trans. 90 (1994) 2965.
[9] R. Schmidt, M. Stöcker, E. Hansen, D. Akporiaye, O.H. Ellestad, Microporous Mater. 3 (1995) 443.
[10] J.H. Petropoulos, Langmuir 12 (1996) 4814.
[11] P.I. Ravikovitch, A.V. Neimark, Langmuir 16 (2000) 2419.
[12] K. Schumacher, P.I. Ravikovitch, A. Du Chesne, A.V. Neimark, K.K. Unger, Langmuir 16 (2000) 4648.
[13] K. Morishige, H. Fujii, M. Uga, D. Kinukawa, Langmuir 13 (1997) 3494.
[14] M. Thommes, R. Köhn, M. Fröba, Stud. Surf. Sci. Catal. 128 (2000) 259.
[15] M. Thommes, R. Köhn, M. Fröba, J. Phys. Chem. B 104 (2000) 7932.
[16] R. Schmidt, M. Stöcker, D. Akporiaye, E.H. Torstad, A. Olsen, Microporous Mater. 5 (1995) 1.
[17] V. Alfredsson, M.W. Anderson, Chem. Mater. 8 (1996) 1141.
[18] V. Alfredsson, M.W. Anderson, T. Ohsuna, O. Terasaki, M. Jacob, M. Bojrup, Chem. Mater. 9 (1997) 2066.
[19] T. Wärnheim, A. Jönsson, J. Colloid Interface Sci. 125 (1988) 627.
[20] X. Auvray, C. Petipas, R. Anthore, I. Rico, A. Lattes, J. Phys. Chem. 93 (1989) 7458.
[21] S.S. Funari, G. Rapp, J. Phys. Chem. B 101 (1997) 732.

[22] A. Monnier, F. Schüth, Q. Huo, D. Kumar, D. Margolese, R.S. Maxwell, G.D. Stucky, M. Krishnamurty, P. Petroff, A. Firouzi, M. Janicke, B.F. Chmelka, Science 261 (1993) 1299.
[23] J.C. Vartuli, K.D. Schmitt, C.T. Kresge, W.J. Roth, M.E. Loenowicz, S.B. McCullen, S.D. Hellring, J.S. Beck, J.L. Schlenker, D.H. Olson, E.W. Sheppard, Chem. Mater. 6 (1994) 2317.
[24] C.A. Fyfe, G. Fu, J. Am. Chem. Soc. 117 (1995) 9709.
[25] Q.H. Huo, D.I. Margolese, G.D. Stucky, Chem. Mater. 8 (1996) 1147.
[26] W.Z. Zhang, T.J. Pinnavaia, Catal. Lett. 38 (1996) 261.
[27] A. Sayari, Chem. Mater. 8 (1996) 1840.
[28] M.S. Morey, A. Davidson, G.D. Stucky, J. Porous Mater. 5 (1998) 195.
[29] M. Morey, A. Davidson, G. Stucky, Microporous Mater. 6 (1996) 99.
[30] K.A. Koyano, T. Tatsumi, Chem. Commun. (1996) 145.
[31] A. Corma, Q. Kan, F. Rey, Chem. Commun. (1998) 579.
[32] W.S. Ahn, D.H. Lee, T.J. Kim, J.H. Kim, G. Seo, R. Ryoo, Appl. Catal. A: Gen. 181 (1999) 39.
[33] M. Anpo, H. Yamashita, K. Ikeue, Y. Fujii, S.G. Zhang, Y. Ichihashi, D.R. Park, Y. Suzuki, K. Koyano, T. Tatsumi, Catal. Today 44 (1998) 327.
[34] J.V. Walker, M. Morey, H. Carlsson, A. Davidson, G.D. Stucky, A. Butler, J. Am. Chem. Soc. 119 (1997) 6921.
[35] M. Morey, A. Davidson, H. Eckert, G. Stucky, Chem. Mater. 8 (1996) 486.
[36] P. Van Der Voort, M. Morey, G.D. Stucky, M. Mathieu, E.F. Vansant, J. Phys. Chem. B 102 (1998) 585.
[37] S. Kawi, M. Te, Catal. Today 44 (1998) 101.
[38] D.Y. Zhao, D.J. Goldfarb, J. Chem. Soc., Chem. Commun. (1995) 875.
[39] J. Xu, Z. Luan, M. Hartmann, L. Kevan, Chem. Mater. 11 (1999) 2928.
[40] H. Kosslick, G. Lischke, H. Landmesser, B. Parlitz, W. Storek, R. Fricke, J. Catal. 176 (1998) 102.
[41] R. Schmidt, H. Junggreen, M. Stöcker, Chem. Commun. (1996) 875.
[42] A.A. Romero, M.D. Alba, J. Klinowski, J. Phys. Chem. B 102 (1998) 123.
[43] B. Echchahed, A. Moen, D. Nicholson, L. Bonneviot, Chem. Mater. 9 (1997) 1716.
[44] M. Hartmann, S. Racouchot, C. Bischof, Chem. Commun. (1997) 2367.
[45] A. Reller, S. Ebbinghaus, R. Köhn, M. Fröba, U. Sazama, P. Fortunato, Mater. Res. Soc. Symp. Proc. 547 (1999) 75.
[46] M.S. Morey, G.D. Stucky, S. Schwarz, M. Fröba, J. Phys. Chem. B 103 (1999) 2037.
[47] L.-Z. Wang, J.-L. Shi, W.-H. Zhang, M.-L. Ruan, J. Yu, D.-S. Yan, Chem. Mater. 11 (1999) 3015.
[48] M. Fröba, R. Köhn, G. Bouffaud, O. Richard, G. van Tendeloo, Chem. Mater. 11 (1999) 2858.
[49] R. Köhn, G. Bouffaud, O. Richard, G. van Tendeloo, M. Fröba, Mater. Res. Soc. Symp. Proc. 547 (1999) 81.
[50] R. Köhn, F. Brieler, M. Fröba, Stud. Surf. Sci. Catal. 129 (2000) 341.
[51] E.P. Barrett, L.G. Joyner, P.P. Halenda, J. Am. Chem. Soc. 73 (1951) 373.
[52] T. Ressler, J. Synchrotron Rad. 5 (1998) 118.
[53] J.J. Rehr, J. Mustre de Leon, S.I. Zabinsky, R.C. Albers, J. Am. Chem. Soc. 113 (1991) 5135.
[54] B. Marler, U. Oberhagemann, S. Vortmann, H. Gies, Microporous Mater. 6 (1996) 375.
[55] W. Hammond, E. Prouzet, S.D. Mahanti, T.J. Pinnavaia, Microporous Mesoporous Mater. 27 (1999) 19.
[56] U. Ciesla, F. Schüth, Microporous Mesoporous Mater. 27 (1999) 131.
[57] A. Saito, H.C. Foley, AIChE J. 37 (1991) 429.
[58] A. Saito, H.C. Foley, Microporous Mater. 3 (1995) 531.
[59] K.S.W. Sing, D.H. Everett, R.A.W. Haul, L. Mouscou, R.A. Pierotti, J. Rouquerol, T. Siemieniewska, Pure Appl. Chem. 57 (1985) 603.
[60] R.L. Blake, R.E. Hessevick, T. Zoltai, L.W. Finger, Am. Mineral 51 (1966) 123.
[61] R.M. Cornell, U. Schwertmann, The Iron Oxides, VCH Verlagsgesellschaft, Weinheim, 1996.
[62] M. Fröba, O. Muth, Adv. Mater. 11 (1999) 564.
[63] C. Minchev, R. Köhn, T. Tsoncheva, M. Dimitrov, M. Fröba, Stud. Surf. Sci. Catal. (2001), in press.